

Quasi-periodic Slipping Magnetic Reconnection During an X-class Solar Flare Observed by the *Solar Dynamics Observatory* and *Interface Region Imaging Spectrograph*

Ting Li & Jun Zhang

ABSTRACT

We firstly report the quasi-periodic slipping motion of flare loops during an eruptive X-class flare on 2014 September 10. The slipping motion was investigated at a specific location along one of the two ribbons and can be observed throughout the impulsive phase of the flare. The apparent slipping velocity was 20–110 km s⁻¹ and the associated period was 3–6 min. The footpoints of flare loops appeared as small-scale bright knots observed in 1400 Å, corresponding to fine structures of the flare ribbon. These bright knots were observed to move along the southern part of the longer ribbon and also exhibited a quasi-periodic pattern. The Si IV 1402.77 Å line was redshifted by 30–50 km s⁻¹ at the locations of moving knots with a ~40–60 km s⁻¹ line width, larger than other sites of the flare ribbon. We suggest that the quasi-periodic slipping reconnection is involved in this process and the redshift at the bright knots is probably indicative of reconnection downflow. The emission line of Si IV at the northern part of the longer ribbon also exhibited obvious redshifts of about 10–70 km s⁻¹ in the impulsive phase of the flare, with the redshifts at the outer edges of the ribbon larger than those in the middle. The redshift velocities at post-flare loops reached about 80–100 km s⁻¹ in the transition region.

Subject headings: magnetic reconnection — Sun: flares — Sun: filaments, prominences

1. Introduction

Solar flares result from the abrupt release of magnetic energy via the process of magnetic reconnection (Parker 1957; Zweibel & Yamada 2009). Eruptive flares are accompanied by

Key Laboratory of Solar Activity, National Astronomical Observatories, Chinese Academy of Sciences, Beijing 100012, China; [liting;zjun]@nao.cas.cn

coronal mass ejections (CMEs) that constitute major drivers for space weather (Bothmer & Schwenn 1994; Forbes et al. 2006). The classical two-dimensional (2D) magnetic reconnection model called the CSHKP model (e.g., see the review of Shibata & Magara 2011) has been developed to explain some characteristics of eruptive flares, including the formation of coronal flux ropes (e.g., Sakurai 1976), flare ribbons (e.g., Schmieder et al. 1996) and post-flare loops (e.g., Milligan & Dennis 2009). Flare ribbons are correlated with the impact of energetic particles launched from the reconnection site underlying the eruptive flux rope with the chromosphere (Asai et al. 2004; Reid et al. 2012; Zhang et al. 2014). The velocity behavior measured in chromospheric ribbons is blueshifted surrounded by redshifts due to the post-flare loops material (Schmieder et al. 1987). After the reconnection the material is cooling and descending along the loops. In $H\alpha$ the velocity along the post-flare loops is of the order of $100\text{--}150\text{ km s}^{-1}$ (Schmieder et al. 1996; Wiik et al. 1996; van Driel-Gesztelyi et al. 1997). It is nearly the free fall value.

However, the 2D CSHKP model can not completely explain the intrinsic three-dimensional (3D) nature and the complex evolution of eruptive flares, such as the formation of the sigmoid (Green et al. 2011), double J-shaped ribbons and strong-to-weak shear transition in post-flare loops (Aulanier et al. 2012). Recently, 3D extensions to the CSHKP model have been proposed by Aulanier et al. (2012) and Janvier et al. (2013). They have presented the 3D magnetohydrodynamic (MHD) evolution process of the flux rope ejection and the slipping motion of field lines in 3D reconnection. Magnetic field lines undergo a continuous series of reconnections as they cross the quasi-separatrix layers (QSLs; Priest & Démoulin 1995; Démoulin et al. 1996), where field line linkage displays a rapid change but is not necessarily discontinuous as in separatrices. The continuous restructuring of field lines along the QSLs results in the apparent slipping motion of field line footpoints (Aulanier et al. 2005). Depending on the velocity of the slipping motion, two definitions were given in Aulanier et al. (2006): if the velocity is sub-Alfvénic, this is the so-called slipping reconnection, while if the velocity is super-Alfvénic, such slipping field lines correspond to the slip-running reconnection regime.

The observational studies about slipping magnetic reconnection are very rare until now, although the theoretical models have been well developed. Aulanier et al. (2007) and Dudík et al. (2014) respectively investigated the apparent slipping motions of bright coronal loops in active region (AR) and flare loops during an eruptive flare, supporting the existence of slipping magnetic reconnection. Based on the *Solar Dynamics Observatory* (SDO; Pesnell et al. 2012) observations, Li & Zhang (2014) reported the slipping motion of flare loops during the eruption of a flux rope. Different from previous studies, the slipping motion of flare loops in this work shows a quasi-periodic pattern. Here, the quasi-periodic pattern means that the appearance of flare loops and their subsequent slipping motion are intermittent. The recently

launched *Interface Region Imaging Spectrograph* (*IRIS*; De Pontieu et al. 2014) mission is now providing observations of the transition region (TR) and the chromosphere with remarkable spatial and spectral resolution. Here, we present the first simultaneous imaging and spectroscopic observations of quasi-periodic slipping magnetic reconnection based on *SDO* and *IRIS* data.

2. Observations and Data Analysis

The Atmospheric Imaging Assembly (AIA; Lemen et al. 2012) onboard the *SDO* uninterruptedly observes the full disk of the Sun in 10 (E)UV channels at $1''.5$ resolution and 12 s cadence. We use the observations of 131, 94, 171, 193 and 1600 Å on 2014 September 10 to investigate the evolutions of flare loops and ribbons. The full-disk line-of-sight magnetograms from the Helioseismic and Magnetic Imager (HMI; Scherrer et al. 2012) are also applied. The *IRIS* observations were taken from 11:28 UT to 17:58 UT, with the field of view (FOV) covering the majority of the NOAA AR 12158. The slit-jaw images (SJIs) centered at 1400 Å are used to analyze the fine-scale structures of flare ribbons, with $0''.33$ – $0''.4$ spatial resolution and a cadence of ~ 19 s (De Pontieu et al. 2014). The spectral data are taken in a sit-and-stare mode with 9 s cadence and a spectral dispersion of ~ 0.026 Å pixel $^{-1}$. The emission line of Si IV is mainly analyzed. The Si IV 1402.77 Å line is formed in the middle TR with a temperature of about $10^{4.9}$ K (Tian et al. 2014a; Li et al. 2014). Since the profile of Si IV 1402.77 Å line is close to Gaussian to some extent, we applied a single-Gaussian fit to the 1402.77 Å line (Peter et al. 2014) and obtained the temporal evolution of peak intensity, Doppler shift, and line width (Figures 4 and 5).

3. Results

3.1. Overview of the X1.6 Flare

On 2014 September 10, an X1.6 flare occurred in the sigmoidal region NOAA AR 12158 (Cheng et al. 2015), including an η -shaped negative-polarity flare ribbon (north part as NNR and south part SNR in Figures 1(g)-(h)) and a semicircular positive-polarity ribbon (PR in Figures 1(g)-(h)) surrounding the sunspot. The GOES soft X-ray 1–8 Å flux showed that the X1.6 flare initiated at 17:21 UT, reached its peak at 17:45 UT (Figure 3(d)). Two groups of loop systems (“G1” and “G2” in Figure 1; see Animation 131-slippage) observed at 131 Å and 94 Å were involved in the flare. During the flare evolution, more flare loops successively appeared and the two loop systems “G1” and “G2” both exhibited apparent slipping motions.

The south footpoints of “G1” gradually propagated towards the southwest (panels (a)-(f)), which develops into the ribbon SNR (panels (h)-(i)). Similarly, the south footpoints of “G2” slipped to the southwest (panels (a)-(f)) and corresponded to the propagation of the NNR (panels (h)-(i)). The flare loops generally refer to the hot coronal loops that are formed between the two ribbons, the counterpart of the loops that belong to the CME and that stay in the lower atmosphere (they used to be called post-flare loops). However, the flare loops in this work are moving to the tip of the ribbons and these are not post-flare loops.

3.2. Quasi-periodic Slipping Motion

Immediately at the start of the flare, the flare loops of the system “G1” exhibited the apparent slipping motion (Figures 2(a)-(b)), and their footpoints developed into the SNR (panels (c)-(d)). The fine-scale structures of the SNR could be observed in *IRIS* 1400 Å images, appearing as numerous dot-like features (panels (e)-(h); see Animation 1400-ribbon). These small-scale knots were seen to appear intermittently and propagate along the ribbon towards the southwest (diamond and circle symbols in panels (e)-(h)). In order to analyze the kinematic evolution of the slipping loops in AIA EUV channels in detail, we obtain the stack plots in different wavelengths (Figures 3(a)-(c)) along the straight line “A–B” (Figure 1(f)). The stack plots show multiple moving intensity features, with each strip representing the apparent slippage of flare loops. The motion of flare loops was fast in the early stage, with an apparent velocity of about 110 km s^{-1} (white dotted line in panel (b)). Afterwards, the slippage became slow and the slipping velocity decreased to $20\text{--}30 \text{ km s}^{-1}$ (blue dotted lines in panel (b)). Here, the appearance of flare loops and their slippage are intermittent, and indeed somewhat periodic, but each time it is not the same “clump” of brightness that is seen, but new flare loops. About six strips were observed between 17:32 UT and 17:56 UT in the stack plot of 131 Å (panel (b)). The time intervals between two neighboring strips ranged from 3.3 min to 6.3 min, and the average period was about 4.8 min (panel (d)). These bright features are seen to move for a period of several to 10 min and their propagating distance were 10–22 Mm.

The quasi-periodic slipping motions are best seen at 94 and 131 Å (panels (a)-(b)) and are not obvious in lower-temperature EUV wavelengths (panel (c)). The 94 and 131 Å channels respectively correspond to high temperatures of about 7 MK and 11 MK, and the 171 Å is at about 0.6 MK (O’Dwyer et al. 2010). In the stack plot of 171 Å, the bright features are blurred and only four strips could be discerned (panels (c) and (f)). The early peaks in each light curve (panels (d) and (f)) appear at a similar place, however, the late peaks are not consistent due to the decreasing intensity of flare loops at 94 and 171 Å. To

study the evolution of moving knots along the SNR, we construct the stack plot at 1400 Å (Figure 3(e)) along the straight line “C–D” (Figure 2(d)). The stack plot exhibits a similar quasi-periodic pattern, with several approximately parallel strips of enhanced intensity. The moving velocity of bright knots is similar to the slipping velocity of flare loops. Seen from the 1400 Å stack plot, the intersections of the slipping knots along the SNR with the stationary slit of *IRIS* spectral observations could be clearly identified. The six diamonds in the stack plot denote the time when the moving knots arrived at the slit position.

To investigate the spectral characteristics of the moving knots along the SNR, we use a Gaussian function to fit the profiles of Si IV 1402.77 Å line and display the temporal evolution of the Gaussian fit parameters in Figure 4. The temporal evolutions of peak intensity, Doppler shift, and line width are in the slit range between the two red horizontal bars in Figure 2(d). The six red arrows in Figure 4 strictly correspond to the times of six diamonds (Figure 3(e)) in the stack plot, when the slipping knots arrived at the slit position. Thus we deduce that each wave-like structure in Figure 4 is indicative of the process that a moving knot passes by the slit position. A total of eight peaks could be discerned between 17:33 UT and 17:56 UT. The redshift exhibits a trend of an increase at the locations of the moving knots. Before the appearance of the knot in the slit, the redshift is about 10–20 km s⁻¹. This value increases to about 30–50 km s⁻¹ near the peak time. The line width of Si IV at the location of the SNR shows a similar trend. At the arrival of the slipping knot, the line profile becomes broader and the width increases to 40–60 km s⁻¹.

3.3. Spectroscopic Properties of the NNR and Post-flare Loops

Similar to the SNR, the NNR also exhibits obvious redshifts in Si IV 1402.77 Å line (Figure 5). In the impulsive phase of the flare (between 17:21 and 17:45 UT), the NNR expanded in opposite directions along the slit position and the ribbon became wider. Along the slit, we select four locations: three corresponding to the NNR and one at the background without flare ribbons (Figure 5(a)). The profiles of the Si IV line at these locations and their Gaussian fittings are shown in Figure 5(e). For the spectral profiles at some locations of the NNR are saturated in the impulsive phase, the value of Doppler shift obtained by Gaussian fitting is not exact and the uncertainty is estimated according to the 1-sigma error in GAUSSFIT function. The redshift velocities at the outer edges of the NNR are respectively 33 ± 2 and 66 ± 20 km s⁻¹ (red and yellow curves), larger than the velocity in the middle of the ribbon (25 km s⁻¹; black curves). The temporal evolution of the Doppler shift in the impulsive phase shows that the Si IV line is always redshifted at the NNR, with values of about 10–70 km s⁻¹ (panel (g)). By examining the spectroscopic observations of

other emission lines of Mg II, C II and Fe XII, we find that these lines mainly exhibit obvious redshift at the NNR, similar to the Si IV line.

In the gradual phase of the flare (starting from 17:45 UT), the peak intensities of the Si IV line and redshift velocities both exhibit a significant decrease (panels (e)-(f)). The maximum intensity was at the southernmost edge of the NNR and the redshift was only 11 km s^{-1} at 17:56 UT (yellow curves in panel (f)). The larger redshifts of $20\text{--}40 \text{ km s}^{-1}$ appeared at the north part of the NNR (red and black curves in panel (f)). Starting from 17:52 UT, post-flare loops were formed as seen in SJI 1400 Å images (panel (b)). The emission of the Si IV line at the post-flare loops also shows an obvious redshift (blue curves in panel (f)). The redshift velocities in the TR were about $80\text{--}100 \text{ km s}^{-1}$ (panels (f)-(g)), within the range of the reconnection outflow speed (Liu et al. 2013; Yang et al. 2015).

4. Summary and Discussion

We firstly report the observations of the quasi-periodic slipping motion of flare loops during an X1.6 flare by the *SDO* and *IRIS* on 2014 September 10. The slipping motion appeared in one location along the SNR throughout the impulsive phase of the flare. The associated period was 3–6 min and the speed of the apparent slipping motion ranged from 20 to 110 km s^{-1} . The footpoints of slipping loops were a series of bright knots that simultaneously underwent a quasi-periodic slipping motion along the flare ribbon. The spectroscopic observations of the *IRIS* showed that the redshifts of Si IV 1402.77 Å line at the locations of moving knots were larger than other locations of the flare ribbon, with a value of about $30\text{--}50 \text{ km s}^{-1}$. Similarly, the line profile became broader at the locations of slipping knots and the width increased to $40\text{--}60 \text{ km s}^{-1}$. For the NNR, the Si IV 1402.77 Å line exhibited obvious redshifts of about $10\text{--}70 \text{ km s}^{-1}$ in the impulsive phase and the redshifts at the outer edges of the ribbon were larger than those in the middle. The post-flare loops were formed in the gradual phase of the flare and the Si IV line was redshifted by $\sim 80\text{--}100 \text{ km s}^{-1}$ near the loop footpoints.

The slipping is only an apparent motion since the connectivity of magnetic field lines is continuously changing within the QSLs due to a succession of reconnection between neighboring field lines (Janvier et al. 2013; Dudík et al. 2014). The slipping motion of flare loops shows a quasi-periodic pattern, indicating the occurrence of quasi-periodic slipping reconnection. The slippage of flare loops at the same location reappeared for several times, with a time interval of 3–6 min. Dynamic models of magnetic reconnection predict that the tearing mode instability and coalescence of magnetic islands recur intermittently (Ofman et al. 1991; Kliem et al. 2000), resulting in the generation of oscillatory reconnection.

The triggering of magnetic reconnection and modulation of its rate can be affected by fast MHD waves (Nakariakov & Melnikov 2009; McLaughlin et al. 2009), hence the magnetic reconnection shows oscillatory dynamics. Heggland et al. (2009) presented that the waves propagating upward from the photosphere/convection zone induce periodic reconnection of the magnetic field. Chen & Priest (2006) proposed that p-mode oscillations can induce oscillatory reconnection by modulating the plasma density near the reconnection site. In our observations, the period of the oscillatory reconnection is 3–6 min, which approximately corresponds to the period of solar p-mode waves. One possible explanation is that the p-mode oscillations above the sunspots in AR 12158 may cause the variation of the plasma density near the reconnection site and the reconnection rate oscillates accordingly (Chen & Priest 2006). Thus the slipping magnetic reconnection appears in a quasi-periodic way and the slipping motion of flare loops is intermittent and quasi-periodic.

In the flare ribbons, the *IRIS* emission lines (Mg II, C II, Si IV and Fe XII) all exhibited significant redshifts (the Si IV line for 10–70 km s⁻¹). Redshifts measured in plasma of the TR are usual in plages (Klimchuk 1989; Simon et al. 1986; Malherbe et al. 1987). The velocity measured in the middle of bright ribbons is blueshifted (Schmieder et al. 1987; Berlicki et al. 2005). In the impulsive phase of the flare, the hot emission lines at temperatures of several MK mostly exhibited blueshifts with speeds of several hundred km s⁻¹ while cool emission lines were redshifted by tens of km s⁻¹ (del Zanna et al. 2006; Li & Ding 2011; Ning 2011; Tian et al. 2014b). In our work, the redshifted ribbons in the TR probably imply the downward-moving cool and dense chromospheric and TR condensations (Fisher et al. 1985) during the impulsive phase and the early stage of the gradual phase.

Many thanks to Hardi Peter, Hui Tian, Le-Ping Li and Li-Mei Yan for discussion about data analysis. *IRIS* is a NASA small explorer mission developed and operated by LMSAL with mission operations executed at NASA Ames Research center and major contributions to downlink communications funded by the Norwegian Space Center (NSC, Norway) through an ESA PRODEX contract. We acknowledge the *SDO/AIA* and HMI for providing data. This work is supported by the National Basic Research Program of China under grant 2011CB811403, the National Natural Science Foundations of China (11303050, 11025315, 11221063 and 11003026), the CAS Project KJCX2-EW-T07 and the Strategic Priority Research Program—The Emergence of Cosmological Structures of the Chinese Academy of Sciences, Grant No. XDB09000000.

REFERENCES

- Asai, A., Yokoyama, T., Shimojo, M., et al. 2004, *ApJ*, 611, 557
- Aulanier, G., Golub, L., DeLuca, E. E., et al. 2007, *Science*, 318, 1588
- Aulanier, G., Janvier, M., & Schmieder, B. 2012, *A&A*, 543, A110
- Aulanier, G., Pariat, E., & Démoulin, P. 2005, *A&A*, 444, 961
- Aulanier, G., Pariat, E., Démoulin, P., & DeVore, C. R. 2006, *Sol. Phys.*, 238, 347
- Berlicki, A., Heinzel, P., Schmieder, B., Mein, P., & Mein, N. 2005, *A&A*, 430, 679
- Bothmer, V., & Schwenn, R. 1994, *Space Sci. Rev.*, 70, 215
- Chen, P. F., & Priest, E. R. 2006, *Sol. Phys.*, 238, 313
- Cheng, X., Ding, M. D., & Fang, C. 2015, arXiv:1502.07801
- Démoulin, P., Henoux, J. C., Priest, E. R., & Mandrini, C. H. 1996, *A&A*, 308, 643
- del Zanna, G., Berlicki, A., Schmieder, B., & Mason, H. E. 2006, *Sol. Phys.*, 234, 95
- De Pontieu, B., Title, A. M., Lemen, J. R., et al. 2014, *Sol. Phys.*, 289, 2733
- Dudík, J., Janvier, M., Aulanier, G., et al. 2014, *ApJ*, 784, 144
- Fisher, G. H., Canfield, R. C., & McClymont, A. N. 1985, *ApJ*, 289, 434
- Forbes, T. G., Linker, J. A., Chen, J., et al. 2006, *Space Sci. Rev.*, 123, 251
- Green, L. M., Kliem, B., & Wallace, A. J. 2011, *A&A*, 526, A2
- Hegglund, L., De Pontieu, B., & Hansteen, V. H. 2009, *ApJ*, 702, 1
- Janvier, M., Aulanier, G., Pariat, E., & Démoulin, P. 2013, *A&A*, 555, A77
- Kliem, B., Karlický, M., & Benz, A. O. 2000, *A&A*, 360, 715
- Klimchuk, J. A. 1989, *Sol. Phys.*, 119, 19
- Lemen, J. R., Title, A. M., Akin, D. J., et al. 2012, *Sol. Phys.*, 275, 17
- Li, L. P., Peter, H., Chen, F., & Zhang, J. 2014, *A&A*, 570, 93
- Li, T., & Zhang, J. 2014, *ApJ*, 791, L13

- Li, Y., & Ding, M. D. 2011, *ApJ*, 727, 98
- Liu, W., Chen, Q., & Petrosian, V. 2013, *ApJ*, 767, 168
- Malherbe, J. M., Schmieder, B., Mein, P., & Tandberg-Hanssen, E. 1987, *A&A*, 172, 316
- McLaughlin, J. A., De Moortel, I., Hood, A. W., & Brady, C. S. 2009, *A&A*, 493, 227
- Milligan, R. O., & Dennis, B. R. 2009, *ApJ*, 699, 968
- Nakariakov, V. M., & Melnikov, V. F. 2009, *Space Sci. Rev.*, 149, 119
- Ning, Z. 2011, *Sol. Phys.*, 273, 81
- O’Dwyer, B., Del Zanna, G., Mason, H. E., Weber, M. A., & Tripathi, D. 2010, *A&A*, 521, A21
- Ofman, L., Chen, X. L., Morrison, P. J., & Steinolfson, R. S. 1991, *Physics of Fluids B*, 3, 1364
- Parker, E. N. 1957, *J. Geophys. Res.*, 62, 509
- Pesnell, W. D., Thompson, B. J., & Chamberlin, P. C. 2012, *Sol. Phys.*, 275, 3
- Peter, H., Tian, H., Curdt, W., et al. 2014, *Science*, 346, 1255726
- Priest, E. R., & Démoulin, P. 1995, *J. Geophys. Res.*, 100, 23443
- Reid, H. A. S., Vilmer, N., Aulanier, G., & Pariat, E. 2012, *A&A*, 547, A52
- Sakurai, T. 1976, *PASJ*, 28, 177
- Schmieder, B., Forbes, T. G., Malherbe, J. M., & Machado, M. E. 1987, *ApJ*, 317, 956
- Schmieder, B., Heinzl, P., van Driel-Gesztelyi, L., & Lemen, J. R. 1996, *Sol. Phys.*, 165, 303
- Scherrer, P. H., Schou, J., Bush, R. I., et al. 2012, *Sol. Phys.*, 275, 207
- Shibata, K., & Magara, T. 2011, *Living Reviews in Solar Physics*, 8, 6
- Simon, G., Schmieder, B., Demoulin, P., & Poland, A. I. 1986, *A&A*, 166, 319
- Tian, H., DeLuca, E., Reeves, K. K., et al. 2014a, *ApJ*, 786, 137
- Tian, H., Li, G., Reeves, K. K., et al. 2014b, *ApJ*, 797, L14

van Driel-Gesztelyi, L., Wiik, J. E., Schmieder, B., et al. 1997, *Sol. Phys.*, 174, 151

Wiik, J. E., Schmieder, B., Heinzl, P., & Roudier, T. 1996, *Sol. Phys.*, 166, 89

Yang, S., Zhang, J., & Xiang, Y. 2015, *ApJ*, 798, L11

Zhang, J., Li, T., & Yang, S. 2014, *ApJ*, 782, L27

Zweibel, E. G., & Yamada, M. 2009, *ARA&A*, 47, 291

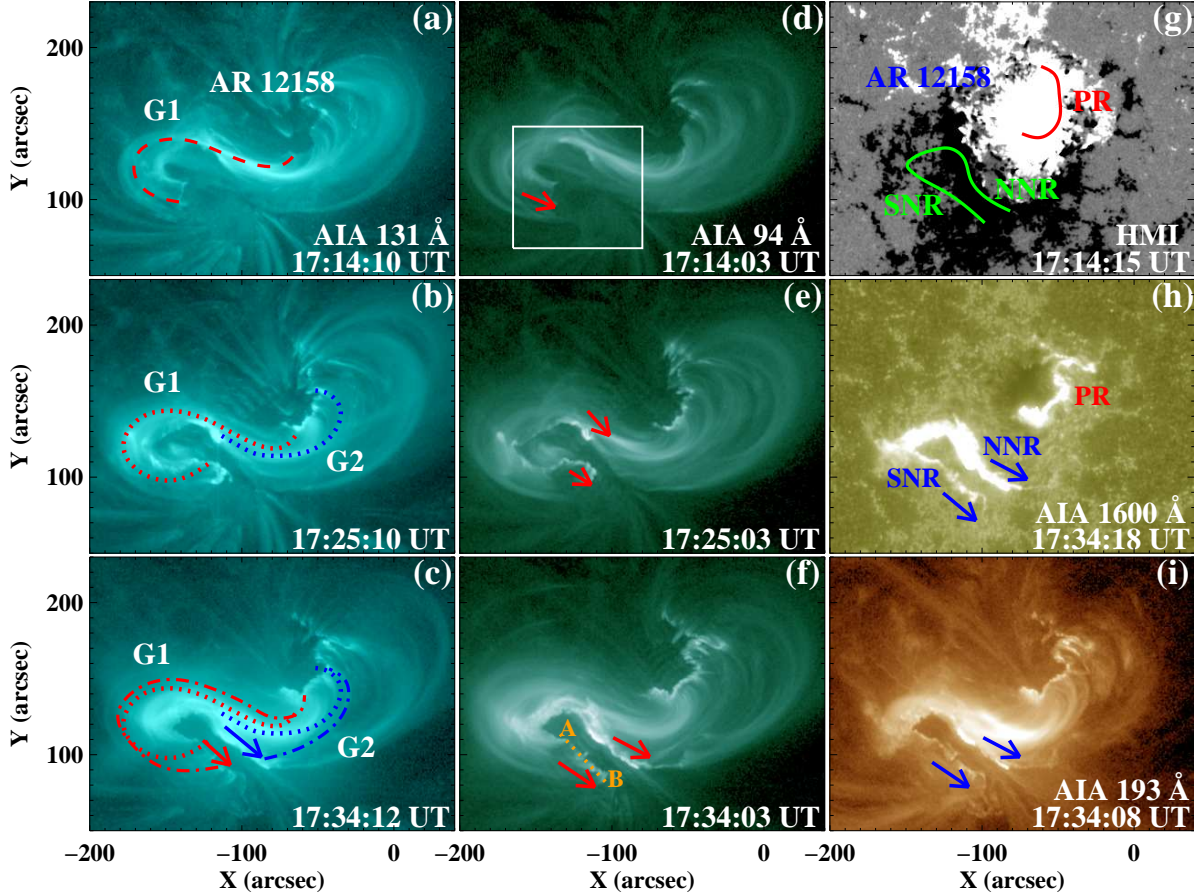


Fig. 1.— Evolution of flare loops and flare ribbons (PR, NNR and SNR) during the X1.6 flare on 2014 September 10 (see Animation 131-slippage). “G1” and “G2” in panels (a)-(c) represent two groups of slipping flare loops. Dotted lines in panel (c) are the duplicates of the flare loops in panel (b). The arrows point to the propagating directions of NNR and SNR. The white rectangle in panel (d) denotes the FOV of Figures 2(a)-(d). Dotted line “A–B” (panel (f)) shows the cut position used to obtain the stack plots shown in Figures 3(a)-(c). Red and green curves in panel (g) denote the ribbons PR, NNR and SNR. The arrows in panels (h) and (i) show the propagating directions of NNR and SNR.

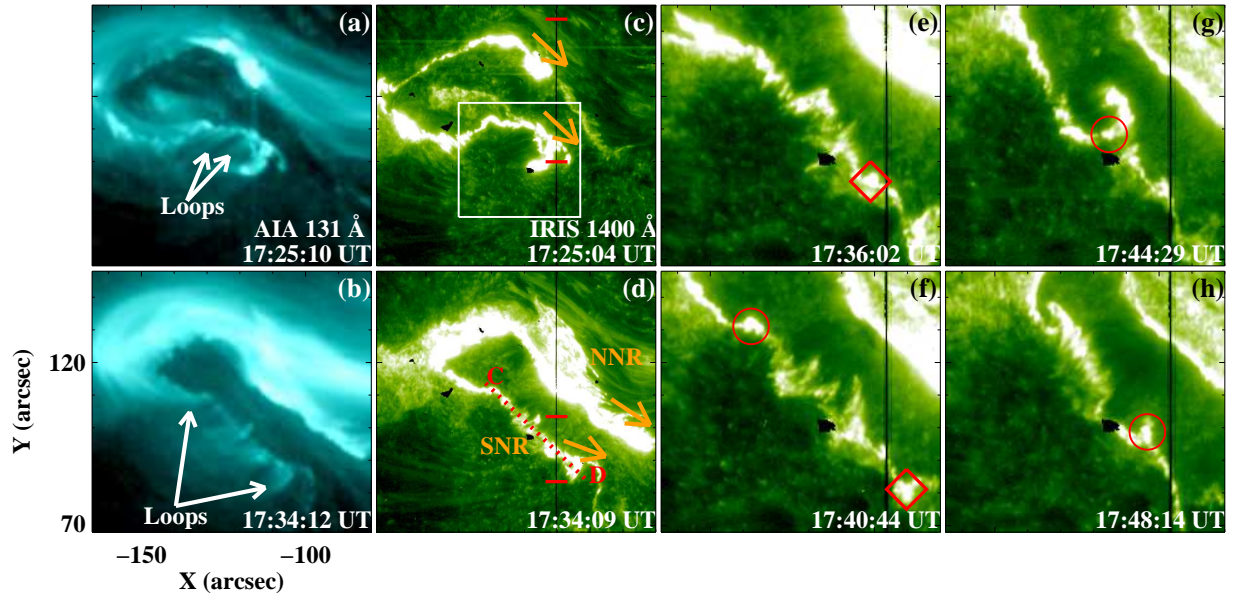


Fig. 2.— AIA 131 Å (panels (a)-(b)) and *IRIS* 1400 Å images (panels (c)-(h)) showing the slipping loops and fine structures of the flare ribbon (see Animation 1400-ribbon). White rectangle in panel (c) denotes the FOV of panels (e)-(h). Dotted line “C–D” (panel (d)) shows the cut position used to obtain the stack plot shown in Figure 3(e). The two red horizontal bars in panels (d) and (c) respectively indicate the spatial range shown in Figures 4 and 5. The diamonds and circles (panels (e)-(h)) outline two propagating bright knots along the SNR.

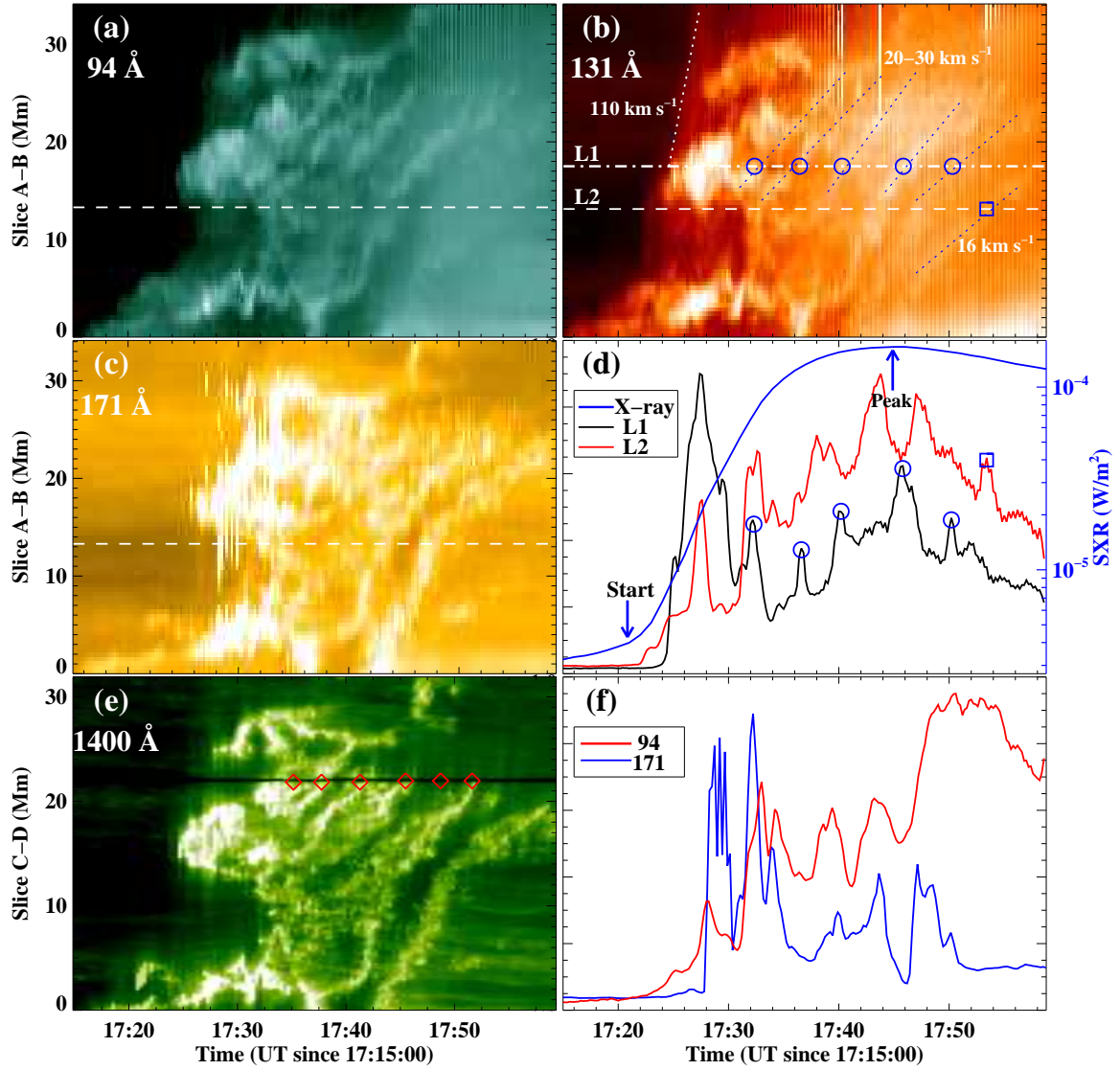


Fig. 3.— Panels (a)-(c): stack plots along slice “A–B” (yellow dotted line in Figure 1(f)) in different wavelengths showing the quasi-periodic slipping motion. Blue circles and square in panel (b) denote the intersections of blue dotted lines with two horizontal lines (“L1” and “L2”). Panel (d): GOES SXR 1–8 Å flux (blue curve) of the associated flare and horizontal slices (black and red curves) along the dash-dotted (“L1”) and dashed lines (“L2”) in panel (b). Blue circles and square are the duplicates of symbols in panel (b). Panel (e): stack plot along slice “C–D” (red dotted line in Figure 2(d)) at 1400 Å showing the evolution of the SNR. The six diamonds denote the time when the moving knots arrive at the slit position. Panel (f): horizontal slices along the dashed lines in stack plots of 94 and 171 Å.

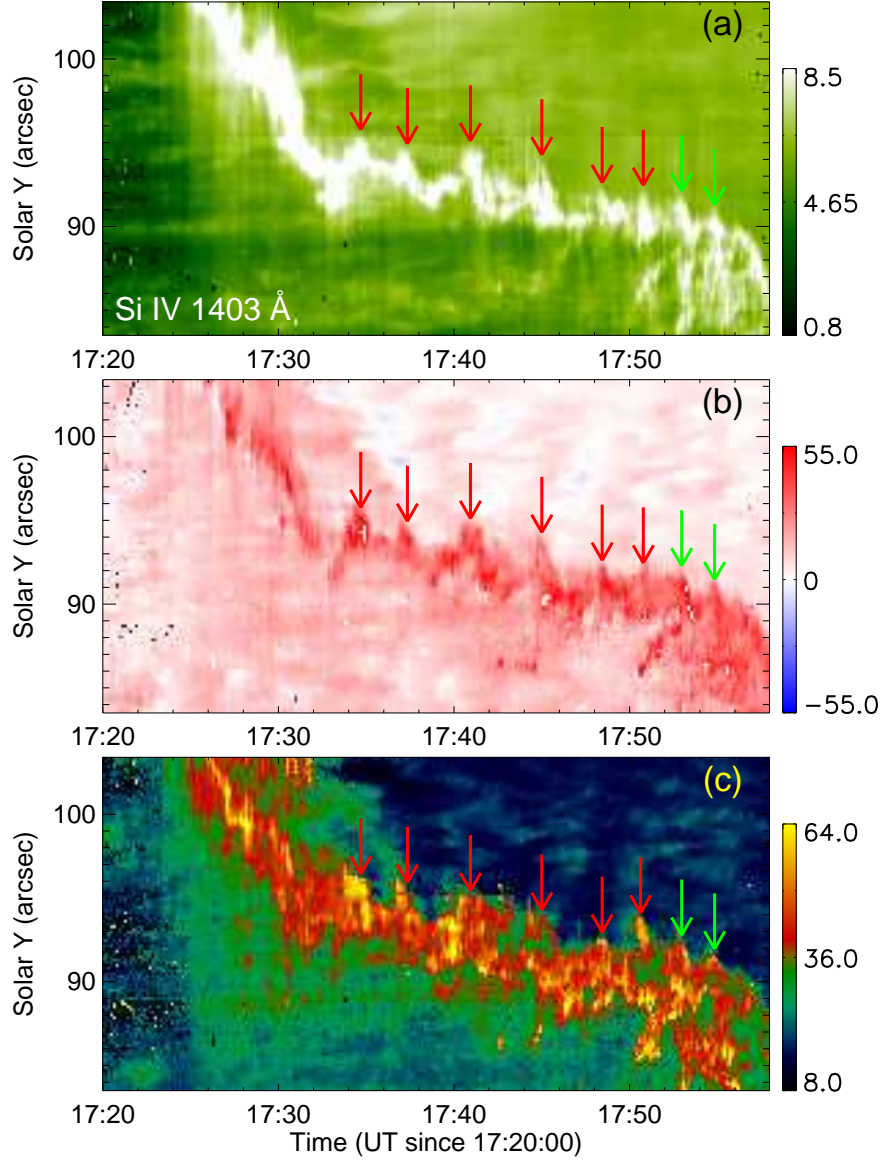


Fig. 4.— Temporal evolution of peak intensity (a), Doppler shift (b), and line width (c) in the spatial range indicated by the two red horizontal bars in Figure 2(d). These parameters are obtained by applying single-Gaussian fits to the Si IV 1402.77 Å line. The arrows point to the peaks of wave-like evolution and correspond to the times when the slipping knots pass by the location of the *IRIS* slit (the six red arrows correspond to the six diamonds in Figure 3(e); two green arrows are not observed in the stack plot of 1400 Å for the propagating direction of the SNR is away from the slice “C–D”).

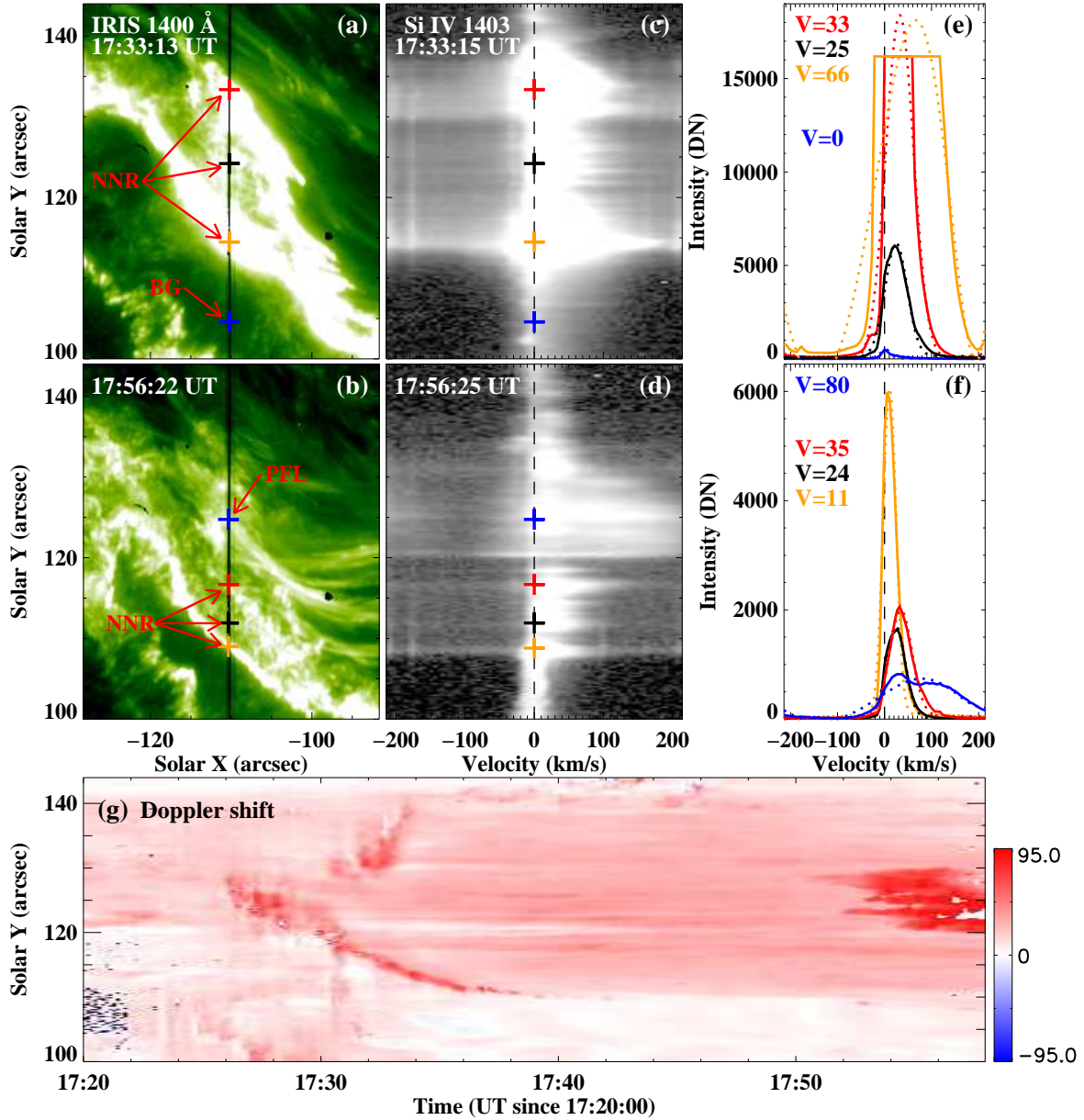


Fig. 5.— Panels (a)-(b): *IRIS* 1400 Å images showing the NNR and the post-flare loops (PFL). The range of y axis is between the two red horizontal bars in Figure 2(c). The red, black and yellow pluses in panels (a) and (b) denote the three locations in the NNR. The blue plus (BG) in panel (a) indicates one location at the background without flare ribbons, and the blue one (PFL) in panel (b) displays the intersection of the PFL with the slit. Panels (c)-(d): evolution of the Si IV 1402.77 Å spectra in the slit range of panels (a)-(b). Panels (e)-(f): profiles of the Si IV line at the NNR, BG and PFL. The dotted curves are the Gaussian fitting profiles. Panel (g): temporal evolution of the Si IV Doppler shift at the NNR and PFL. The spatial range is the same as that of panels (a)-(d).